

PAPER • OPEN ACCESS

## Impedance matched electrical capacitance tomography system: front-end design and system analysis

To cite this article: M Flatscher *et al* 2019 *Meas. Sci. Technol.* **30** 104002

View the [article online](#) for updates and enhancements.

You may also like

- [A high-efficiency management circuit for weak piezoelectric energy harvester](#)  
P Li, Y M Wen, Q Zhou et al.
- [Segmented impact-type piezoelectric energy harvester for self-start impedance matching circuit](#)  
Hyun Jun Jung, Soobum Lee, Sinwoo Jeong et al.
- [Analytic Mapping between Porous Electrode Theory and Equivalent Circuit](#)  
Klemen Zeli, Ivo Panik, Miran Gaberscek et al.

# Impedance matched electrical capacitance tomography system: front-end design and system analysis

M Flatscher<sup>✉</sup>, M Neumayer<sup>✉</sup> and T Bretterkieber<sup>✉</sup>

Institute of Electrical Measurement and Measurement Signal Processing Graz University of Technology, 8010 Graz, Austria

E-mail: [matthias.flatscher@tugraz.at](mailto:matthias.flatscher@tugraz.at)

Received 14 January 2019, revised 21 May 2019

Accepted for publication 30 May 2019

Published 12 August 2019



## Abstract

Electrical capacitance tomography (ECT) is a well-established technique for process monitoring, which enables the visualization of spatial material distributions within a region of interest, e.g. a pipeline. Switched capacitor (SC) circuits or continuous displacement current measurements are used to measure the coupling capacitances within the ECT sensor. In order to measure the coupling capacitances with high accuracy, the circuit concepts make use of fast excitation signals, e.g. fast transients in SC circuits or high excitation frequency signals in continuous displacement current measurements. For industrial process tomography in harsh environments a spatial separation between the sensor and the front-end circuitry is favorable. Consequently, the measurement circuitry and the sensor are connected by means of coaxial cables. For high excitation frequencies, transmission line effects like standing waves, reflections, or impedance transformation effects appear, leading to undefined signal conditions in the measurement system. It can be shown that the undefined signal propagation can lead to significant measurement errors. In this paper we present an impedance matched front-end circuitry, i.e. the source impedance of the excitation source and the input impedance of the measurement circuitry are matched to the wave impedance of the transmission lines. Due to the matching the signal propagation becomes defined, allowing the use of arbitrary cable lengths and excitation signals. We present the design of an impedance matched front-end for ECT and study the behavior of the excitation system and the measurement system. Comparative measurements from a demonstrator are presented. Finally we study the measurement error of the system and show the validity of the impedance matched system approach.

Keywords: electrical capacitance tomography, transmission lines, RF measurement, impedance matched design

(Some figures may appear in colour only in the online journal)

## 1. Introduction

Process tomography is a measurement approach to monitor the quality and quantity of goods in industrial processes [1]. It is of great interest for process optimization [2]. Several

tomographic process monitoring techniques have been suggested [3]. A suitable measurement technique for process monitoring in industrial processes is electrical capacitance tomography (ECT) [4]. ECT is an imaging technique, which is based on capacitance measurements. Hereby the spatial distribution of the dielectric material properties is visualized. It can be applied for processes material with a low conductivity [5]. The application of ECT has been reported in different applications, reaching from monitoring of multi phase flows



Original content from this work may be used under the terms of the [Creative Commons Attribution 3.0 licence](https://creativecommons.org/licenses/by/3.0/). Any further distribution of this work must maintain attribution to the author(s) and the title of the work, journal citation and DOI.

[6], monitoring of fluidized beds [7] or monitoring of pneumatic conveying processes [8, 9].

Figure 1 depicts a sketch of a typical ECT measurement system used for process tomography. The sensor consists of a non-conductive pipe, which encloses the region of interest (ROI). Electrodes are mounted at the outside of the pipe and are surrounded by a shield [10].

The measurement quantities for an ECT sensor are the inter-electrode capacitances between the individual electrodes. Based on the measured inter-electrode capacitances, the spatial permittivity distribution within the region of interest can be visualized by solving an ill-posed inverse measurement problem [11–13]. The solution of the inverse problem requires measurements of high quality, e.g. high signal to noise ratio (SNR) and resolution [14], as well as an accurate model of the measurement process [15]. To measure the coupling capacitance between two electrodes, one electrode is attached to the transmitter (TX), which provides an excitation signal. The inter-electrode capacitance can then be determined by measuring the displacement current at the other electrode, which is connected to the receiver (RX). Dedicated analog signal conditioning structures are usually needed for ECT systems and are tailored according to specific measurement demands. Various authors have suggested different measurement techniques to determine the inter-electrode capacitance, e.g. switched capacitor (SC) techniques [16, 17] or continuous displacement current measurements [18–22] have been proposed. For the receiver system low-impedance input stages (charge amplifiers or current to voltage converters) are widely used, as these architecture shows good immunity to input stray capacitances [23–25]. To obtain a required signal strength, the addressed measurement techniques maintain different strategies. In switched capacitor techniques high excitation voltages are used, e.g. in [16] an excitation voltage of up to 200V is referred. Continuous displacement current measurement systems maintain higher excitation frequencies [26], e.g. in [18] an excitation frequency of 40 MHz is used.

As the ECT measurement circuitry has to determine the coupling capacitance between the electrodes, the impact of stray capacitances has to be considered. The influence of these capacitances can be reduced by mounting the circuitry close to the sensor, e.g. the electronics and the electrodes are directly connected. In this case the measurement of the coupling capacitance is well defined, i.e. the measurement process provides the correct coupling capacitance. To maintain a small error between the measured inter-electrode capacitances and the capacitances obtained by the model, the boundary conditions must be sufficiently known, i.e. the excitation voltage amplitude applied to the electrodes. Usually calibration techniques are applied to further reduce the error caused by this deviation [27–29]. Systems with a short connection between the measurement circuitry and the electrodes have been published by various authors, e.g. [18, 30]. For process tomography in industrial environments, a directly attached assembly is unfavorable, as it leads to an exposure of the measurement electronics to harsh conditions, e.g. high temperatures or high pressure. To increase the system lifetime and reliability, a spatial separation of the sensor and the vulnerable measurement

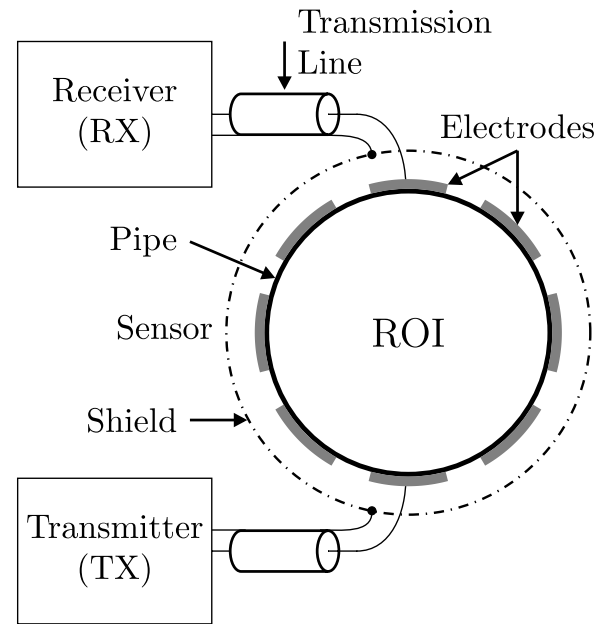


**Figure 1.** Simplified illustration of an ECT measurement setup with transmission lines to connect the sensor and the measurement electronics. The sensor encloses the region of interest.

electronics is preferred. Consequently, the measurement circuitry and the sensor electrodes are connected by means of coaxial cables as depicted in figure 1.

The coaxial cables are referred to as transmission lines [31] and cannot be represented by a lumped capacitor if high excitation frequencies are used [32]. Transmission line effects like standing waves, impedance transformation properties and signal reflections appear within the measurement system [33]. These effects appear in both, switched capacitor and continuous displacement current measurement systems. In switched capacitor systems reflections are caused due to fast transients of the excitation signal [34]. The signal propagation and therefore the measurement process is not well defined. The excitation voltage at the electrodes varies due to the transmission line effects. In [35] the influence of the instrumentation system has been studied for different continuous displacement current measurements. Note, that wave propagation effects can also appear within the sensor. However, it has been found that wave propagation effects within the sensor require significantly higher frequencies than the used measurement frequencies. In [36] wave propagation effects in the sensor have been found to be significant for frequencies, which are an order of magnitude higher than the suggested measurement frequencies used in ECT systems.

In this paper we present an impedance matched front-end design for ECT, which is based on continuous displacement current measurements. This article is an extended version of [33]. The source impedance of the transmitter and the input impedance of the receiver are matched to the wave impedance of the transmission lines, e.g. 50  $\Omega$ . Because of the defined termination impedances no reflection occur and the measurement process becomes well defined. Impedance matched systems are well known and studied in communication systems. However, for an ECT measurement system the source and the

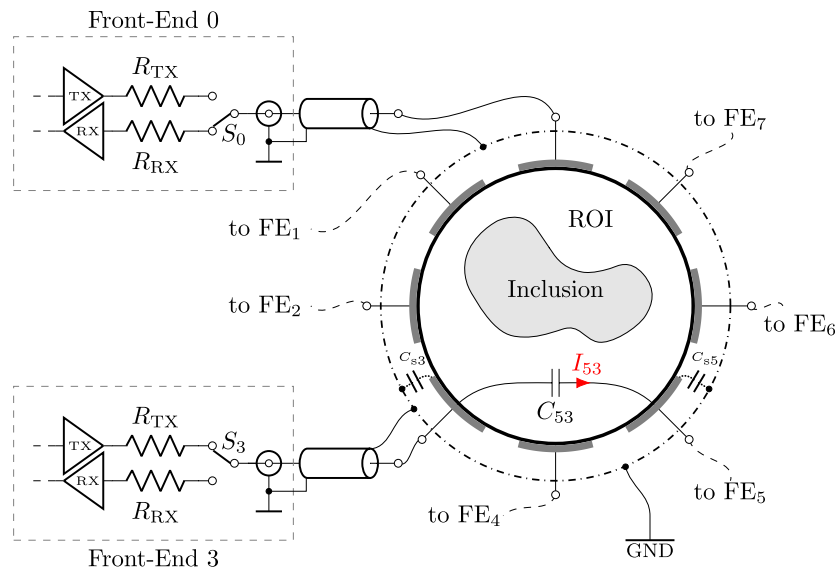


**Figure 2.** Sketch of an ECT configuration consisting of eight (gray) electrodes and front-ends  $FE_i$ , arranged around the circumference of a pipe (black circle). The ECT sensor is surrounded by a screen, which is connected to system ground (GND) and represented by the dash-dotted circle. The transmit- (TX) and receive- (RX) path of each front-end can be changed by means of a switch, as indicated by  $S_0$  and  $S_3$ .  $C_{53}$  represents the coupling capacitance between electrode three and five.

input impedance have an influence on the measurement too, e.g. the receiver input impedance is not low as for the current to voltage converter, but is given by the wave impedance.

The novelty of this work and the main extensions can be summarized by the following contributions.

- Topology of an impedance matched front-end to operate as receiver and transmitter.
- Study of the impedance matched transmitter system.
- Study of an impedance matched receiver system.
- Analysis of the calibration behavior of an impedance matched ECT system.

The paper presents theoretical considerations for the design and the properties on an impedance matched design. The influence of parasitic parameters of the circuit components in the front-end circuitry is addressed. Comparative measurements of a prototype are presented. The measurements show the well defined behavior of the measurement system. The influence of the impedance on the capacitance measurement is studied, showing the applicability of the impedance matched system. The matched front-end allows the use of instrumentation lines with arbitrary length while offering superior signal characteristic compared to a commonly used low impedance system architecture. This is of particular relevance for the development of further systems, e.g. systems with an spectroscopic evaluation principle. We present the functionality of the system for a frequency range up to 50 MHz.

The paper is structured as follows. In section 2 the topology of the front end is studied to realize a combined receiver/transmitter circuitry. In sections 3 and 4 the transmitter system and receiver system is analyzed, respectively. In both sections accompanying measurements are presented. In section 5 a measurement error analysis of the impedance matched system is presented.

## 2. Front-end topology

In this section we discuss general considerations, which have to be taken into account to achieve the desired front-end input/output impedance of  $50 \Omega$ . As can be seen in figure 2, each electrode is attached to an individual front-end ( $FE_i$ ). All front-ends can act as a receiver or transmitter. Therefore, a switch is needed to change between the receiver (RX) and transmitter (TX) path, as indicated by  $S_0$  and  $S_3$  for front-end 0 and 3. To meet the characteristic transmission line impedance  $Z_0$  of  $50 \Omega$ , the output resistance of the transmitter  $R_{TX}$  and the input resistance of the receiver  $R_{RX}$  have to be considered, as well as the on-resistance  $R_{on}$  of the used switch.

### 2.1. Switch selection

As discussed in section 1, the measurement accuracy can be increased either by the usage of high excitation frequencies or high excitation voltages. Systems utilizing high excitation voltages, employ high voltage MOSFETs [37] or mechanical relays [38]. ECT systems operating at high excitation frequencies, enable the use of off the shelf analog switches. There is a variety of radio frequency (RF) switches available, which meet the characteristic wave impedance of  $50 \Omega$ . This switches are usually designed for operating frequency ranges up to several GHz. Therefore the useability of analog switches is investigated in this section.

To minimize high frequency effects, like impedance transformation and standing waves, the front-end is designed to meet the characteristic transmission line impedance  $Z_0$  of  $50 \Omega$ , when operated in receive mode as well as in transmit mode. The input and output resistance  $R_{I/O}$  of each front-end consists of a series connection of the on-resistance  $R_{on}$  of the used switch and an additional output- and input resistor

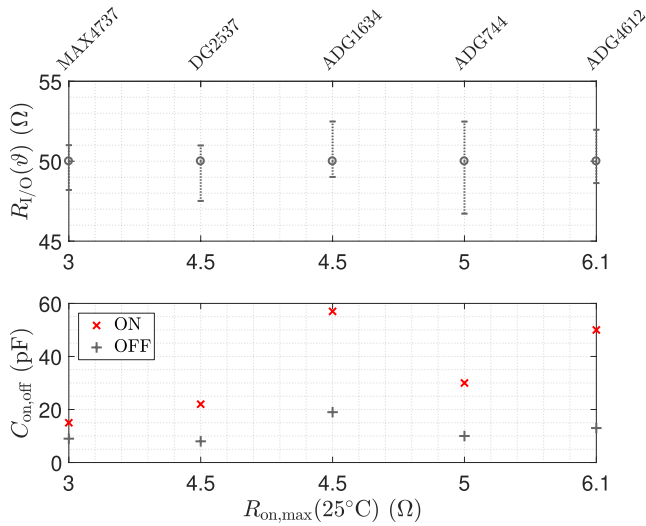


**Figure 3.** Parameters for five different analog switches. Both abscissas show the maximum switch on-resistance  $R_{on,max}(25^\circ\text{C})$  at  $25^\circ\text{C}$ . Upper plot: desired front-end input/output resistance  $R_{I/O}(\vartheta)$  of  $50\ \Omega$  (circles) and its deviation for a temperature range from  $-40^\circ\text{C}$  to  $+85^\circ\text{C}$  according to equation (1). Lower plot: switch on and off capacitance, extracted from the corresponding datasheets.

$R_{TX,RX}$ . These additional resistors are illustrated in figure 2 by  $R_{TX}$  and  $R_{RX}$ . The resistance of  $R_{I/O}$ ,  $R_{on}$  and  $R_{TX,RX}$  depend on the operating temperature  $\vartheta$ . The front-end input/output resistance  $R_{I/O}$  over the temperature  $\vartheta$  can be described by

$$R_{I/O}(\vartheta) = R_{on}(\vartheta) + \underbrace{R_{TX,RX}}_{\pm 1\%} \cdot [1 + \alpha_{\vartheta_0} \cdot (\vartheta - \vartheta_0)] \stackrel{!}{=} 50\ \Omega. \quad (1)$$

The temperature dependent resistance variation of  $R_{TX,RX}$  can be described by its temperature coefficient  $\alpha_{\vartheta_0}$ , specified at reference temperature  $\vartheta_0$  [39]. The on-resistance  $R_{on}(\vartheta)$  of an analog switch increases with the operating temperature  $\vartheta$ . The datasheet of an analog switch usually states three resistance values,  $R_{on,typ}(25^\circ\text{C}) < R_{on,max}(25^\circ\text{C}) < R_{on,max}(\vartheta_{min/max})$ . The typical on-resistance at  $\vartheta = 25^\circ\text{C}$  is denoted by  $R_{on,typ}(25^\circ\text{C})$ ,  $R_{on,max}(25^\circ\text{C})$  represents the maximum on-resistance at  $\vartheta = 25^\circ\text{C}$ , and  $R_{on,max}(\vartheta_{min/max})$  the maximum resistance covering the complete operating temperature range. As the switch on-resistance and  $R_{TX,RX}$  are influenced by the operating temperature  $\vartheta$ , equation (1) cannot be fulfilled over the whole operating temperature range. The upper plot in figure 3 shows  $R_{I/O}(\vartheta)$  and its variation for five different analog switches for a temperature range from  $-40^\circ\text{C}$  to  $+85^\circ\text{C}$ . As the front-end is intended to be operated in industrial environments, where a variation of the ambient temperature can be expected, the maximum switch on-resistance  $R_{on,max}(25^\circ\text{C})$  is used to fulfill equation (1). This leads to the circles in the upper plot in figure 3, which mark the desired  $50\ \Omega$  impedance. Equation (1) takes the switch on-resistance variation into account as well as the temperature dependency of  $R_{TX,RX}$ , with a temperature coefficient  $\alpha_{\vartheta_0}$  of  $\pm 10\ \text{ppm}\ ^\circ\text{C}^{-1}$  specified at a reference temperature of  $\vartheta_0 = 25^\circ\text{C}$ . Furthermore a fabrication based

resistance variation of  $R_{TX,RX}$  by  $\pm 1\%$  is considered, leading to the error-bars shown in the upper plot of figure 3. One promising switch with a minimum resistance variation can be spotted.

Electrical capacitance tomography is based on capacitive measurements, and its system behavior is adversely affected by parasitic capacitances. Thus, the switch on-and off-capacitance  $C_{on,off}$  have to be kept low. This capacitances are shown in the lower plot in figure 3. By demanding a minimum input/output resistance variation as well as minimum parasitic switch capacitances, the model MAX4737 by Maxim Integrated looks to be a suitable choice for the proposed matched ECT front-end.

It should be mentioned that the switches in figure 3 are well chosen, by means of their frequency bandwidth, voltage supply range,  $R_{on}(\vartheta)$  variation, capacitances and maximum continuous current. Especially the maximum continuous current has to be minded, as the current distributed across the switch can obtain high values due to the impedance transformation properties of transmission lines [33]. This aspect will be further discussed in section 3.3.

## 2.2. Switch topology

Although a single switch is used by the front-ends depicted in figure 2, the proposed matched front-end makes use of an individual analog switch for the receive-path and transmit-path, respectively. The use of two individual integrated circuits (not placed in the same package) reduces the crosstalk between RX and TX. Figure 4(a) shows the front-end input/output structure based on figure 2, and three possible switch configurations of a front-end operated in receive mode in figures 4(b)–(d). Each circuit makes use of two individual switches. The receiver switch  $S_{RX}$  is represented by  $R_{on}$  and  $C_{on}$ , and the transmitter switch  $S_{TX}$  by  $C_{off}$ . The on-capacitance of an analog switch is the result of several different capacitances, which are determined by its channel width and length, and terminal connections [40]. Usually the datasheet of an analog switch provides only a single on-capacitance value. Therefore, this value is split up into two equal parts [41]. The dashed connection to system ground in figures 4(b)–(d), represents the virtual ground of the transimpedance amplifier [42], shown in figure 4(a). The circuits in figures 4(b) and (c) are using a dedicated receiver resistor  $R_{RX}$  as well as transmitter resistor  $R_{TX}$ . Configuration (b) and (c) allow the use of two different switches, by means of their on-resistance. The circuit shown in figure 4(d) makes use of a common transceiver resistor  $R_{TRX}$ . For this reason, two identical switches are used to meet the characteristic transmission line impedance.

Figure 5 shows the input impedance magnitude  $|Z_{in,i}|$  and phase  $\phi_{Z_{in,i}}$  as a function of the used excitation frequency  $f_{TX}$ , for all three equivalent circuit diagrams. The trends are determined by fulfilling equation (1) and using the switch chosen in section 2.1. For the topology in figure 4(b), the on-capacitance and off-capacitance of both switches are directly attached to the input of the front-end, which results in an unfavorable frequency dependent impedance trend of  $Z_{in,b}$ , in figure 5. By placing the resistors  $R_{RX}$  and  $R_{TX}$  at the other side of the

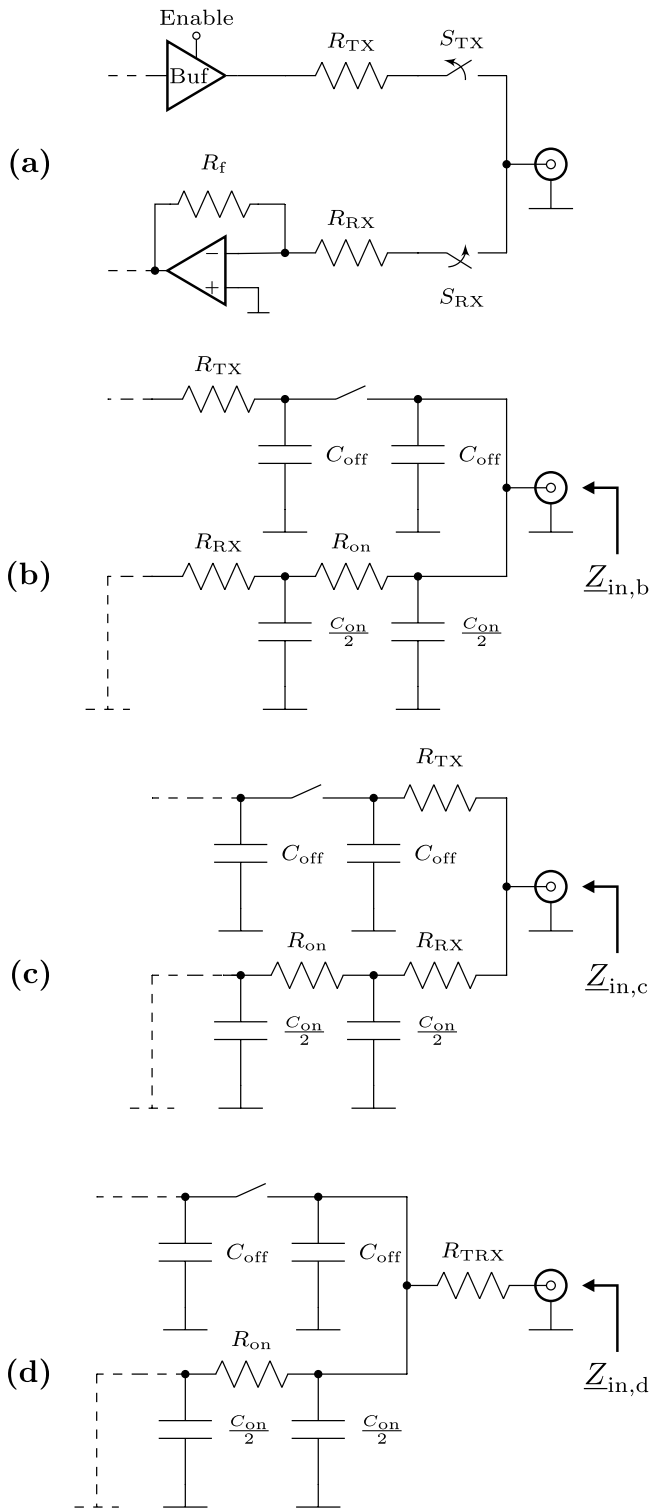


**Figure 4.** (a): Front-end input/output structure based on figure 2. (b)–(d): three different circuit topologies, in order to meet the characteristic transmission line impedance of 50 Ω. The circuits in (b)–(d) are operated in receive mode. Switch  $S_{RX}$  is represented by  $R_{on}$  and  $C_{on}$ , and  $S_{TX}$  by  $C_{off}$ . Circuit (b) and (c) use a dedicated receiver resistor  $R_{RX}$  as well as a transmitter resistor  $R_{TX}$ . Circuit (d) makes use of a common transceiver resistor  $R_{TRX}$ .

switches, as shown in figure 4(c), a better frequency performance is achieved. This is due to the isolation of  $C_{off}$  and  $C_{on}/2$  by  $R_{TX}$  and  $R_{RX}$ , respectively. Nevertheless, as the frequency

increases, the total impedance of the transmit branch ( $C_{off}$ ,  $R_{TX}$ ) decreases. This results in a frequency dependent impedance, which is in parallel with the receive-path. The best performance shows the circuit in figure 4(d), which has an almost constant impedance in the observed frequency range, due to the isolation of the parasitic switch capacitances by a shared transceiver resistor  $R_{TRX}$ . The resistance and phase deviation in the observed frequency range is about 1 mΩ and 0.05°, respectively. The almost frequency independent characteristic indicates the usability of analog switches for the proposed matched front-end.

### 2.3. Proposed front-end

Based on the requirements, discussed in sections 2.1 and 2.2, and results presented in [33] and [43], an impedance matched front-end has been designed. A system sketch is shown in figure 6. The transmit path consists of a direct digital synthesizer (DDS), enabling excitation frequencies up to 50 MHz. The DDS is followed by a reconstruction low pass filter. To provide sufficient current driving capability [33], a buffer (Buf) is used.

The received displacement current is converted into a voltage, by means of a transimpedance amplifier. A variable gain amplifier (VGA) is used as additional gain stage. The amplified measurement signal is filtered and digitized by a high speed analog to digital converter (ADC). As discussed in section 2.2, two individual switches are used to minimize the crosstalk between both paths.

Based on the presented front-end in figure 6, a prototype has been realized. The input/output impedance performance of the transmitter and receiver are investigated in sections 3 and 4 respectively.

## 3. Transmitter

As discussed in section 1, the quality of the reconstruction result depends on the simulation of the measurement process with sufficient accuracy. For the simulation of the measurement process a constant voltage ( $V_{TX}$  in figure 7) is applied in the simulation model. By taking the frond-end output impedance into account, the actual excitation voltage  $V_{Elec}$  applied to the transmit electrode differs from the intended excitation voltage  $V_{TX}$ . To gain knowledge of the expected excitation system behavior, the model depicted in figure 7 is analyzed. Based on figure 2,  $FE_3$  acts as transmitter and is attached to its corresponding electrode by means of a transmission line with length  $l_{cable}$  and impedance  $Z_0$ . Based on the selected switch in section 2.1, the front-end includes a common transceiver surface mounted device (SMD) resistor  $R_{TRX}$  with a resistance of 47 Ω and a case size of 0603. A 0603 SMD resistor has a parasitic inductance of approximately 1.55 nH [44] and capacitance of about 50 fF [45], which are considered as well. The trace inductances  $L_{trc,i}$  shown in figure 7 are a result of the printed circuit board (PCB) layout and the resulting trace length. The trace inductances  $L_{trc,i}$  are determined according to [46] with an inductance per length unit of approximately

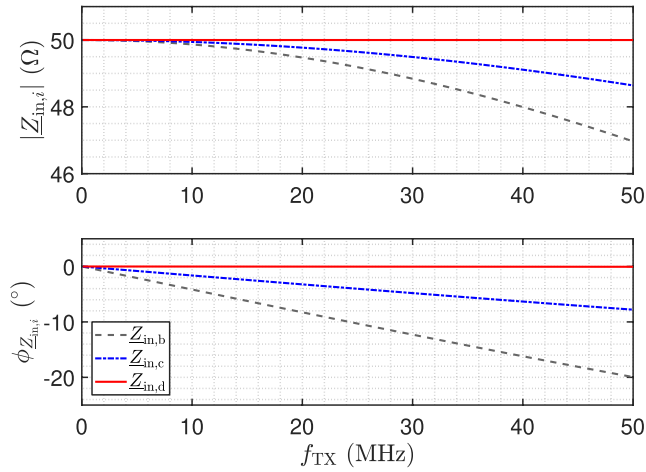


**Figure 5.** Impedance trends for three different switch topologies, shown in figures 4(b)–(d). The upper plot shows the impedance magnitude  $|Z_{in,i}|$ , the lower one its phase  $\phi_{Z_{in,i}}$ .

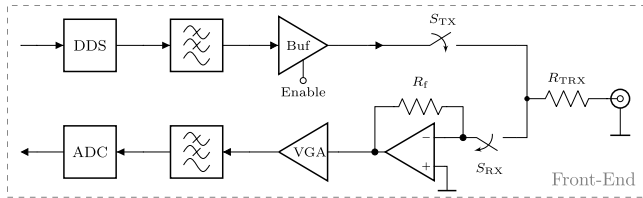


**Figure 6.** Proposed matched measurement front-end. The upper part shows the transmitter, consisting of a direct digital synthesizer (DDS), a reconstruction low pass filter, a buffer (Buf) and a switch  $S_{TX}$ . The receiver in the lower part of the sketch consists of a switch  $S_{RX}$ , a transimpedance amplifier, a variable gain amplifier (VGA), an anti-aliasing filter and an analog to digital converter (ADC). Both paths share a common transceiver resistor  $R_{TRX}$ .

$1 \text{ nH mm}^{-1}$ . The sensor is represented by the capacitive  $\Pi$ -network to the right of the transmission line. The inter-electrode capacitance between  $FE_5$  and  $FE_3$  is depicted by  $C_{53}$ . As indicated in figure 2, stray capacitances ( $C_{s3}$ ,  $C_{s5}$ ) between the screen and the transmit electrode as well as the receive electrode are also considered.  $Z_{RX}$  represents the receiver input impedance of  $FE_5$  and is assumed to be equal  $50 \Omega$ , for the analysis in this section.

Typical inter electrode capacitances range from a few fF up to a few pF [10, 47]. To use capacitance values in the right order of magnitude for the lumped sensor model in figure 7, a finite element method (FEM) simulation of a typical ECT sensor has been performed, resulting in an inter-electrode capacitance  $C_{53}$  of 1 pF and stray capacitances  $C_{s3}$ ,  $C_{s5}$  each with 10 pF [33].

### 3.1. Impedance modeling

The impedance trend of the lumped sensor model shown in figure 7 as well as the measurement results of an actual lumped sensor circuit, realized on a printed circuit board, are shown in figure 8. A network analyzer from Rohde & Schwarz [48] is used to determine the forward reflection coefficient  $S_{11, \text{Sensor}}$  and  $S_{11, \text{TX}}$  of the lumped sensor and the transmitter,

respectively. The sensor impedance  $Z_{\text{Sensor}}$  and the transmitter impedance  $Z_{\text{TX}}$ , shown in figure 7, can be calculated by [31]

$$Z_i = Z_0 \cdot \frac{1 + S_{11,i}}{1 - S_{11,i}}. \quad (2)$$

As can be seen in figure 8, the measured magnitude  $|Z_{\text{Sensor}}|$  and phase  $\phi_{\text{Sensor}}$  are in good agreement with the model based results. The same holds for the transmitter impedance  $Z_{\text{TX}}$  results in figure 9. By having a look on the phase  $\phi_{Z_{\text{TX}}}$ , the positive phase indicates a slight inductive behavior. By including the copper trace inductances  $L_{\text{trc},i}$ , as shown in figure 7, the model exhibits the same characteristic trend.

### 3.2. Electrode voltage

In this paragraph we investigate the relation between the voltage  $V_{\text{TX}}$  at the output of the buffer and the voltage  $V_{\text{Elec}}$  at the transmit electrode of the sensor, as depicted in figure 7. To determine the voltage and current along a transmission line, equations (3) and (4) can be used [49]. Equation (3) is used to determine the voltage  $V_{\text{Elec}}$  (see figure 7), which is applied to the transmit electrode.

$$V(z, z') = V_{\text{con}} \cdot e^{-i\beta z} \cdot \left( \frac{1 + \Gamma_{\text{Sensor}} \cdot e^{-i2\beta z'}}{1 - \Gamma_{\text{TX}} \cdot \Gamma_{\text{Sensor}} \cdot e^{-i2\beta l_{\text{cable}}}} \right) \quad (3)$$

$$I(z, z') = \frac{V_{\text{con}}}{Z_0} \cdot e^{-i\beta z} \cdot \left( \frac{1 - \Gamma_{\text{Sensor}} \cdot e^{-i2\beta z'}}{1 - \Gamma_{\text{TX}} \cdot \Gamma_{\text{Sensor}} \cdot e^{-i2\beta l_{\text{cable}}}} \right). \quad (4)$$

$V_{\text{con}}$  represents the voltage initially sent down the transmission line [49], depicted in figure 7. Given the known excitation source voltage  $V_{\text{TX}}$  at the output of the buffer,  $V_{\text{con}}$  can be determined by initially representing the transmission line by its characteristic impedance  $Z_0$  [49].  $\beta(f_{\text{TX}})$  denotes the excitation frequency dependent phase constant of the transmission line [31]. The distance from the transmitter is denoted by  $z$ , and from the transmit electrode by  $z'$ . The transmission line length is represented by  $l_{\text{cable}}$ . The reflection coefficient of the transmitter  $\Gamma_{\text{TX}}$  and the sensor  $\Gamma_{\text{Sensor}}$  can be calculated by [31]

$$\Gamma_i = \frac{Z_i - Z_0}{Z_i + Z_0}. \quad (5)$$

$Z_0$  denotes the characteristic transmission line impedance of  $50 \Omega$ . The sensor impedance  $Z_{\text{Sensor}}$  and the transmitter impedance  $Z_{\text{TX}}$ , determined in section 3.1, are represented by  $Z_i$  in equation (5).

Figure 10 shows the expected electrode voltage amplitude to excitation voltage amplitude ratio  $V_{\text{Elec}}/V_{\text{TX}}$ , for three different transmission line lengths, based on the derived sensor and front-end model. To validate the models, simultaneous measurements of the electrode voltage and the excitation voltage at the output of the buffer have been conducted by means of an oscilloscope and two active probes. The measurement results in figure 10 are in good match with the model based results. The maximum deviation between the results for a transmission line length of 0.04 m, shown in the upper plot

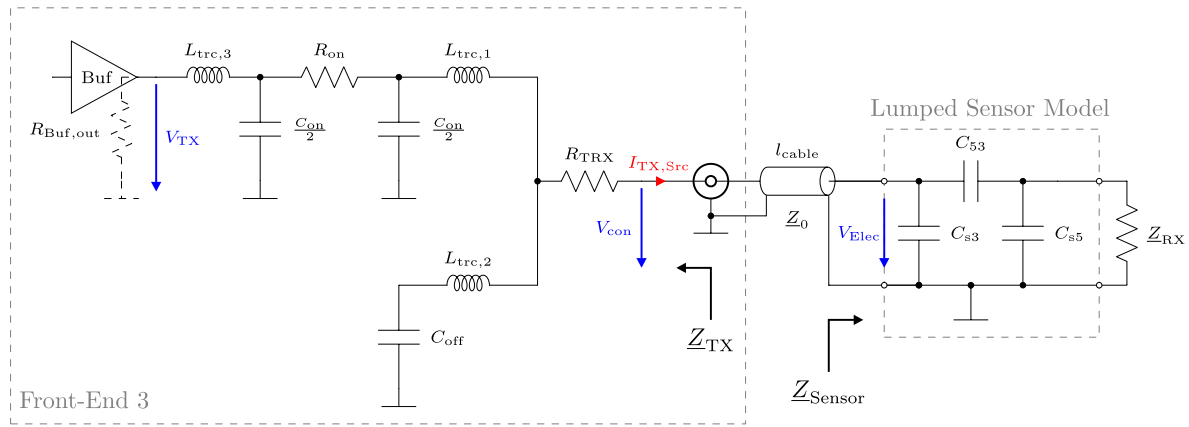


**Figure 7.** Analyzed front-end, operated in transmit mode. The model includes trace inductances  $L_{trc,i}$  as well as the buffer’s output resistance  $R_{Buf,out}$  (see figure 6). The sensor depicted in figure 2, is represented by a lumped  $\Pi$ -network including the receiver input impedance  $Z_{RX}$ . The front-end and the sensor are connected by a transmission line with length  $l_{cable}$  and impedance  $Z_0 = 50 \Omega$ .

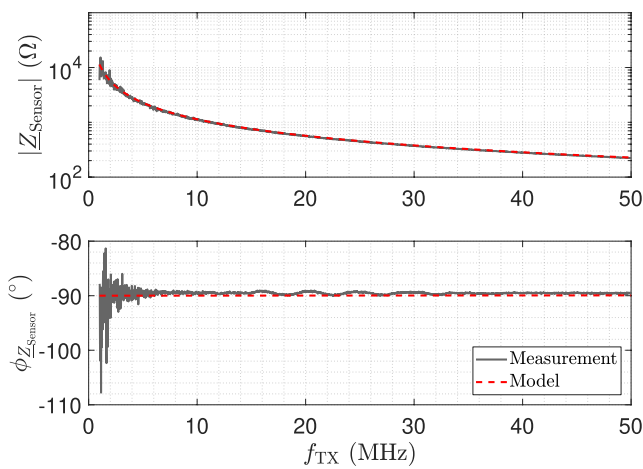


**Figure 8.** Sensor impedance measurement results, determined by a network analyzer, and analytic results for the lumped sensor model shown in figure 7.

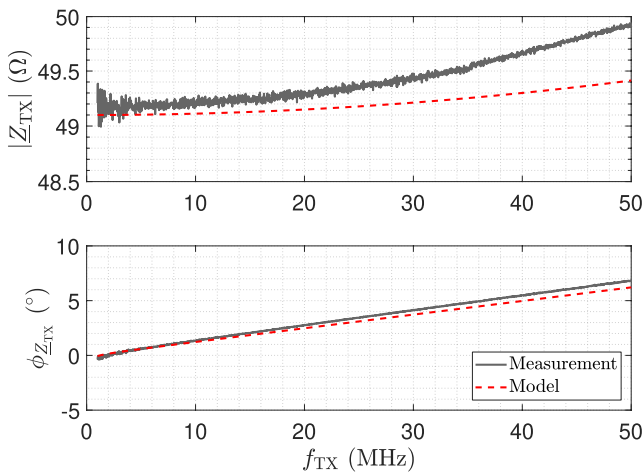


**Figure 9.** Transmitter impedance measurement results, determined by a network analyzer, and analytic results for the front-end model shown in figure 7.

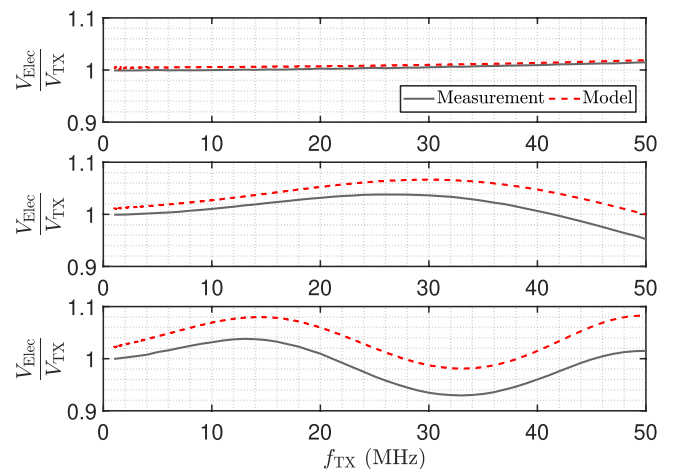


**Figure 10.** Electrode voltage amplitude  $V_{Elec}$  to excitation voltage amplitude  $V_{TX}$  ratio for three different transmission line lengths. Upper plot:  $l_{cable} = 0.04$  m. Middle plot:  $l_{cable} = 1$  m. Lower plot:  $l_{cable} = 2.5$  m. All three plots are showing the analytical result as well as a measurement result, determined by an oscilloscope.

of figure 10, is smaller than 0.5%. By having a closer look at the results for a 1 m long transmission line in the middle plot of figure 10, and for a 2.5 m long transmission line in the lower plot, an offset can be seen. This deviation is caused by the skin effect of the transmission lines [31], which has not been included in our model. The resulting frequency and length dependent signal attenuation is in good agreement with measurement results for a RG174 coaxial cable, stated in [50].

The datasheet of the used RG174 cable cites an impedance of  $50 \Omega \pm 3 \Omega$ , which is not constant over the observed frequency span. Therefore, impedance measurement results of the used cables are included in the model, to allow a meaningful comparison with the measured electrode voltage in figure 10. By using an ideal transmission line with a constant impedance of  $50 \Omega$ , the results in figure 11 can be determined. The light gray shaded area illustrates the expected ratio of

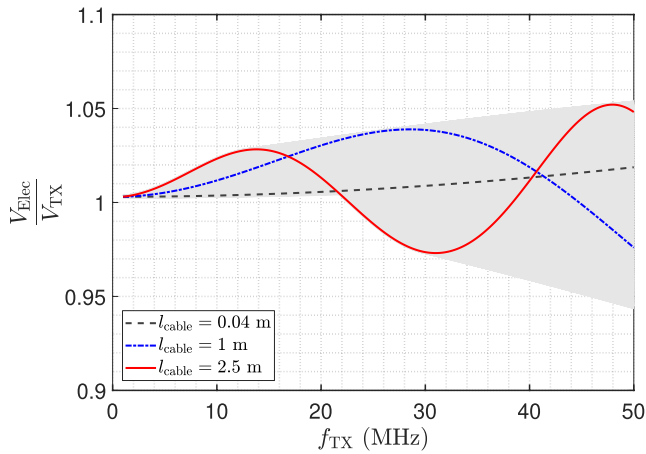


**Figure 11.** Electrode voltage  $V_{\text{Elec}}$  to excitation voltage  $V_{\text{TX}}$  ratio determined for an arbitrary transmission line length between 0 m and 2.5 m, and an ideal transmission line impedance of  $50 \Omega$ .

electrode voltage to excitation voltage  $V_{\text{Elec}}/V_{\text{TX}}$ , for an arbitrary cable length between 0 m and 2.5 m.

### 3.3. Source current

As discussed in section 2.1, the used switches have been chosen with respect to the maximum expected source current  $I_{\text{TX,Src}}$ , flowing across the switch depicted in figure 7. To determine this current, equation (4) is used. Figure 12 shows the model based result and measurement result for the setup illustrated in figure 7, using a transmission line with a length of 2.5 m and an excitation voltage  $V_{\text{TX}}$  amplitude of 2.5 V. Both results show the same characteristic frequency trend. For an excitation frequency close to the quarter-wavelength of the cable, the high sensor impedance is transformed into a short circuit at the other end of the line. This leads to a high source current flow through the chosen switch MAX4737, which has a rated maximum continuous current of 100 mA. As expected, the transmitter output impedance of almost  $50 \Omega$  acts as current limiter [33], resulting in a maximum source current  $I_{\text{TX,Src}}$  amplitude of about 50 mA.

## 4. Receiver

In this section a model of the front-end receiver structure as well as comparative measurement results are presented. As the transmit model presented in section 3, the investigated receiver model shown in figure 13 also includes trace inductances  $L_{\text{trc},i}$  and parasitic elements of the lumped resistors  $R_{\text{TRX}}$  and  $R_f$ . The input impedance performance of the circuit depends among other things on the used operational amplifier, and its ability to keep the voltage difference between its inputs at zero. Therefore, a Spice based modeling approach is used, which allows the integration of the Spice model of the operational amplifier. The realized prototype uses the AD8000 from Analog Devices.

Figure 14 shows the results for a direct attached assembly ( $l_{\text{cable}} = 0 \text{ m}$ ). The input impedance  $Z_{\text{RX}}$  of the circuit is

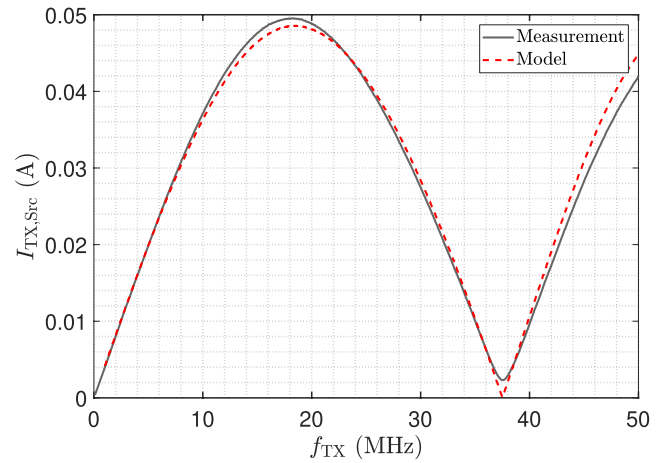


**Figure 12.** Front-end source current  $I_{\text{TX,Src}}$  as a function of the excitation frequency for a cable length of 2.5 m. The excitation voltage  $V_{\text{TX}}$  has an amplitude of 2.5 V.

slightly smaller than the desired  $50 \Omega$ . This is caused by the circuit design considerations according to section 2.1, where the maximum switch on-resistor at  $25^\circ \text{C}$  is used instead of the typical one. As can be seen, the copper trace inductances lead to a slight inductive circuit characteristic.

By connecting the front-end with a transmission line, its input impedance  $Z_{\text{RX}}$  can be represented by its transformed version [31]

$$Z_{\text{RX,tms}} = Z_0 \cdot \frac{Z_{\text{RX}} + i \cdot Z_0 \cdot \tan(\beta \cdot l_{\text{cable}})}{Z_0 + i \cdot Z_{\text{RX}} \cdot \tan(\beta \cdot l_{\text{cable}})}, \quad (6)$$

at the other end of the transmission line, as indicated in figure 13.  $Z_0$  denotes the characteristic transmission line impedance of  $50 \Omega$ .  $\beta(f_{\text{TX}})$  represents the excitation frequency dependent phase constant of the transmission line with a length of  $l_{\text{cable}}$ .  $Z_{\text{RX}}$  is the receiver impedance shown in figure 14. The results for a 2.5 m long transmission line are shown in figure 15. As can be seen, the measurement results are in good agreement with the model, and allows an accurate receiver structure modeling.

As discussed in section 1, the displacement current across the sensor structure (e.g.  $I_{53}$  in figure 2) is used to gain knowledge of the spatial material distribution. The system sketch in figure 2 includes the self capacitance ( $C_{s3}$ ,  $C_{s5}$ ) of the electrode with respect to system ground (GND). The integration of the lumped sensor model from figure 7 in our receiver model shown in figure 13, leads to the simplified circuit in figure 16. As can be seen, the self capacitance  $C_{s5}$  of the receiver electrode creates a current divider with the (transformed) input impedance of the front-end. The transformed receive current to displacement current ratio  $|I_{\text{RX,tms}}/I_{53}|$  of the circuit in figure 16 is illustrated in figure 17.

The current ratio in figure 17 is determined with a transmission line length of 2.5 m. The transformed receive current  $I_{\text{RX,tms}}$  is almost constant for the investigated frequency range. The maximum deviation is about 1% for an excitation frequency of 50 MHz. At this frequency  $C_{s5}$  represents a low impedance, and according to figure 15,  $|Z_{\text{RX,tms}}|$  has

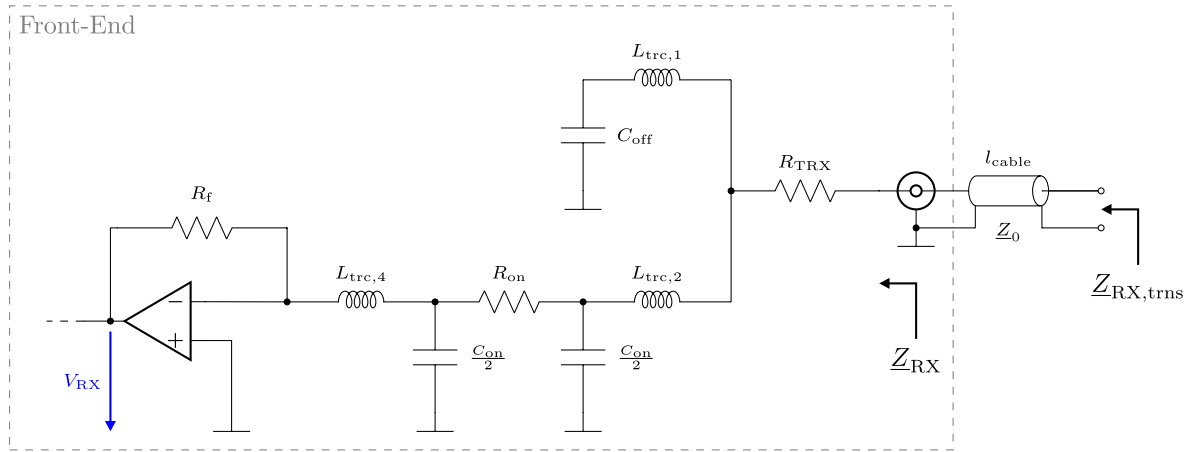


**Figure 13.** Analyzed front-end, operated in receive mode. The model includes trace inductances  $L_{trc,i}$  and the AD8000 operational amplifier Spice model, provided by Analog Devices. The feedback resistor  $R_f$  and the common transceiver resistor  $R_{TRX}$  have a resistance of  $500\ \Omega$  and  $47\ \Omega$ , respectively.

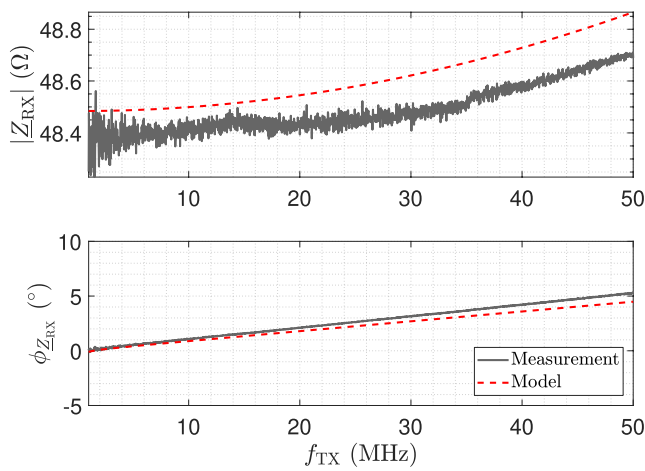


**Figure 14.** Input impedance magnitude  $|Z_{RX}|$  and phase  $\phi_{Z_{RX}}$ , obtained by a measurement and Spice simulation, for a direct attached assembly (0 m).

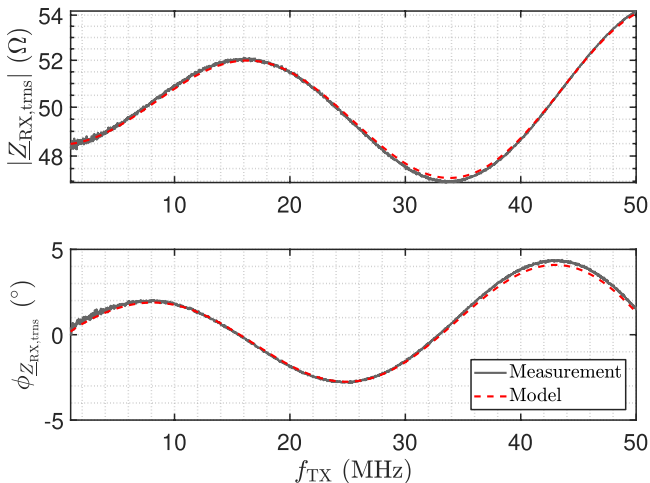


**Figure 15.** Transformed receiver input impedance magnitude  $|Z_{RX,trns}|$  and phase  $\phi_{Z_{RX,trns}}$ , obtained by a measurement and Spice simulation, for a transmission line length of 2.5 m.

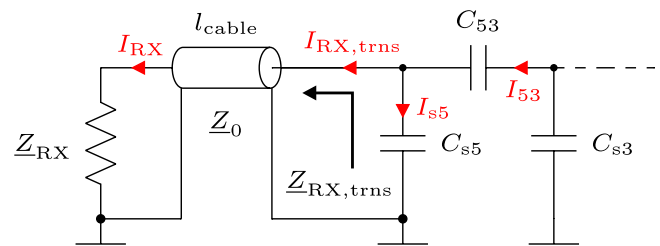


**Figure 16.** Simplified receiver circuit, incorporating the model in figure 13 and the lumped sensor model in figure 7.  $I_{s5}$  represents the displacement current from front-end number 3 to 5, as indicated in figure 2.

its maximum value. The trend in figure 17 indicates a good immunity with respect to the stray capacitance of the receive electrode.

The receive current  $I_{RX}$  at the other end of the transmission line shown in figure 16, can be determined by [49]

$$I_{RX} = \frac{2 \cdot Z_0 \cdot I_{RX,trns}}{(Z_{RX} + Z_0) \cdot e^{i\beta l_{cable}} \cdot [1 - \Gamma_{RX} \cdot e^{-i2\beta l_{cable}}]} \quad (7)$$

$I_{RX,trns}$  is the transformed receive current at the beginning of the transmission line with a length of  $l_{cable}$ .  $\beta(f_{TX})$  represents the excitation frequency dependent phase constant of the transmission line [31].  $Z_0$  denotes the characteristic transmission line impedance of  $50\ \Omega$  and  $Z_{RX}$  the receiver impedance shown in figure 14. The receiver reflection coefficient  $\Gamma_{RX}$  can be determined by equation (5). Figure 18 depicts the normalized receive current change as a function of the excitation frequency  $f_{TX}$ . As can be seen the receive current increases almost linearly.

The receive current  $I_{RX}$  is converted into a corresponding receive voltage  $V_{RX}$  at the output of the operational amplifier, shown in figure 13, by [42]

$$V_{RX} = -R_f \cdot I_{RX} \quad (8)$$

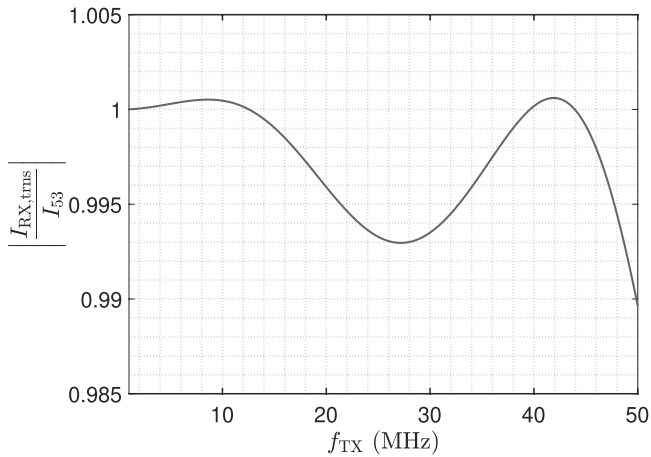


**Figure 17.** Transformed receive current to displacement current ratio according to figure 16. Transmission line length  $l_{\text{cable}}$  is 2.5 m.

$R_f$  is the feedback resistor of the operational amplifier, and  $I_{RX}$  is the receive current at the end of the transmission line shown in figure 16.

## 5. System analysis

In sections 3 and 4 the transmitter and the receiver system have been studied. The results show the desired functionality of each sub system. In this section we provide a study of the error between  $C_{\text{meas}}$  and  $C_{\text{model}}$  for an ECT system when using the impedance matched circuits.  $C_{\text{meas}}$  refers to a measured capacitance,  $C_{\text{model}}$  is the capacitance from the simulation model, which is used for the solution of the inverse problem.

For this study we consider an ECT sensor with an inner diameter of 100 mm and 8 electrodes. The length of the sensor is 100 mm. To compute the influence of the instrumentation system, the capacitance  $C_{\text{model}}$  is computed from the model of the sensor. Following the model calculations, we simulate the measurement system, i.e. the system depicted in figure 1 to compute the measured capacitances  $C_{\text{meas}}$ . For the computation we use scattering matrices of all system components [35]. To compensate the influence of the instrumentation we use the calibration

$$C_{\text{meas,cal}} = C_{\text{model}}(\varepsilon_{\text{low}}) + \frac{C_{\text{model}}(\varepsilon_{\text{high}}) - C_{\text{model}}(\varepsilon_{\text{low}})}{C_{\text{meas}}(\varepsilon_{\text{high}}) - C_{\text{meas}}(\varepsilon_{\text{low}})} (C_{\text{meas}}(\varepsilon_r) - C_{\text{meas}}(\varepsilon_{\text{low}})). \quad (9)$$

Hereby  $\varepsilon_{\text{low}}$  and  $\varepsilon_{\text{high}}$  denote reference measurements and simulations, where the sensor has been filled with a material with a low and a high permittivity, respectively.  $C_{\text{meas,cal}}$  is the calibrated measurement, which is used for the image reconstruction.

The calibration approach given by equation (9) is an offset-gain calibration. This calibration is of practical relevance, as the corresponding calibration experiments can typically be performed with minor effort. For the reference permittivities values  $\varepsilon_{\text{low}}$  and  $\varepsilon_{\text{high}}$  the error  $e = C_{\text{meas,cal}} - C_{\text{model}}$  becomes

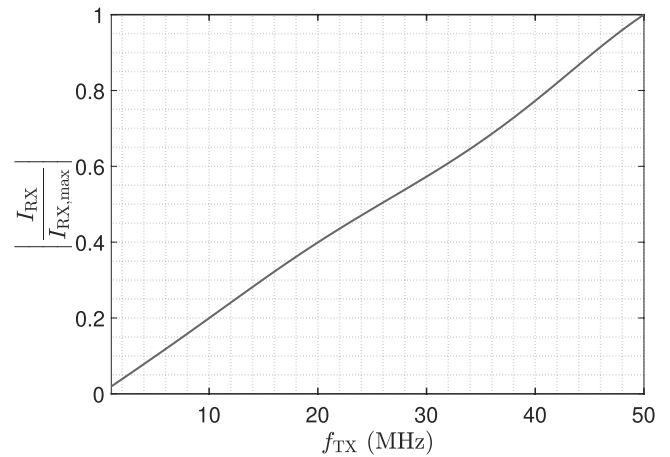


**Figure 18.** Normalized receive current at the exit point of the transmission line with a length  $l_{\text{cable}}$  of 2.5 m, depicted in figure 16.

zero. The trend of  $e$  between the reference points shows the influence of the instrumentation system. This approach allows to evaluate all interactions between the components of the system. For the simulation we use the permittivity value  $\varepsilon_{\text{low}} = 1$  and  $\varepsilon_{\text{high}} = 4$ . The length of the cable is 1 m, the frequency is 40 MHz.

The upper and lower plot in figure 19 depict the relative error  $e_{\text{rel}} = (C_{\text{meas,cal}} - C_{\text{model}})/C_{\text{model}}$  for a near-and a distant electrode pair, respectively. Near and distant electrode refer to the measured coupling capacitance with respect to the electrode used as transmitter. For comparison also the errors of a conventional front-end structure, i.e. a front-end with a current to voltage converter (I/V), are depicted.

With respect to the maximum error for the non-matched current to voltage converter (I/V) design of  $-4.1\%$  for the near electrode pair and  $-0.6\%$  for the distant electrode pair, the matched system error is significantly reduced. The maximum relative measurement error for the matched system is  $0.05\%$  and  $-0.005\%$ , for the near electrode pair and the distant electrode pair, respectively. This is due to the defined measurement process, where no reflections occur. Furthermore, the calibration compensates the influence of the source impedance of the transmitter and the input impedance of the receiver. The result depicted in figure 19 is exemplary with respect to the selected frequency and the transmission line length. We performed several studies for different frequencies and line lengths. The results show the positive impact of the system for all the simulated cases.

## 6. Conclusion

In this paper we presented an impedance matched front-end for ECT applications and an analysis of the system behavior. The impedance matched design refers to the output and input impedance of the transmitter and the receiver system of the front end, respectively. Both impedances equal the wave impedance of the instrumentation lines, e.g.  $50\Omega$ . For ECT

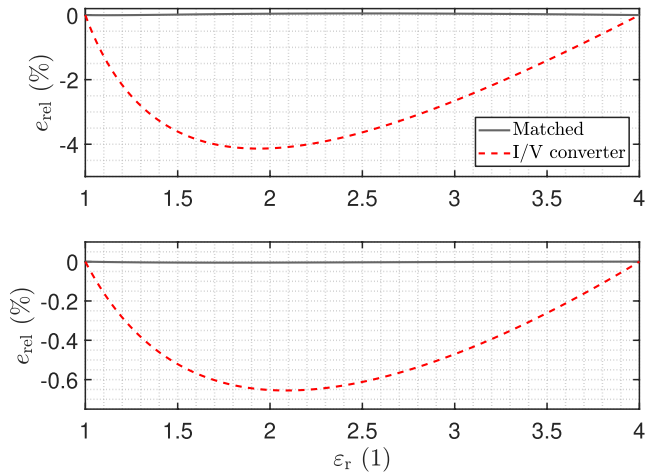


**Figure 19.** Exemplary analysis of the relative measurement error for an impedance matched ECT system, and a current to voltage based (I/V) system. Upper plot: Relative measurement error for a near electrode pair. Lower plot: Relative measurement error for a distant electrode pair. An excitation frequency of 40 MHz and cables with a length of 1 m are used.

front-ends without an impedance matched structure, the signal propagation is not well defined. Wave propagation effects in the instrumentation lines can lead to a significant error for the measured capacitances. The impedance matched system design leads to a defined signal propagation within the measurement system and to a reduced measurement error.

The presented impedance matched front-end can be used for frequencies up to 50 MHz. The transmitter uses a sinusoidal excitation source, the receiver maintains a continuous displacement current measurement. The design of the front-end system has been studied and different front-end topologies are analyzed. For the proposed frequency range parasitic effects of the circuit components have to be considered. We elaborated the critical design parameters of the relevant circuit components and discuss the influence of the front-end behavior by means of simulations. A front-end topology is then suggested, which is suitable for the impedance matched design. The properties of the impedance matched transmitter and receiver are presented and discussed by means of measurements using a prototype circuitry. Measurements for all relevant quantities (signals and system impedances) are presented. The capability of the system to provide the desired behavior, e.g. a constant voltage at the electrode of the sensor over the frequency range is demonstrated for different cable lengths. Also the parasitic influences of the design are discussed and a circuit model for the transmitter and the receiver structure are presented.

The benefit of the system with respect to non-impedance matched designs is demonstrated by means of a system analysis. The characterization of the demonstrator showed the feasibility of the system over a wide frequency range and for different cable lengths. The work provides important aspects for the design of future tomographic measurement systems. Because of the capability to be operated over a wide frequency range and for arbitrary cable lengths the front-end system can

be used for further developments like spectroscopic evaluation systems, where information about the conductivity of the process is used for further process analysis.

## Acknowledgment

This work is funded by the FFG Project (Bridge 1) TomoFlow under the FFG Project Number 6833795 in cooperation with voestalpine Stahl GmbH. Open Access Publication funded by TU Graz Open Access Funds.

## ORCID iDs

M Flatscher  <https://orcid.org/0000-0001-5343-6017>

M Neumayer  <https://orcid.org/0000-0003-1975-8578>

T Bretterklierer  <https://orcid.org/0000-0003-4890-6672>

## References

- [1] Scott D M and McCann H 2005 *Process Imaging for Automatic Control* (Boca Raton, FL: CRC Press)
- [2] Williams R A and Beck M S 1995 *Process Tomography, Principles, Techniques and Applications* (Oxford: Butterworth-Heinemann Ltd.)
- [3] Holder D S 2005 *Electrical Impedance Tomography* 1st edn (Bristol: Institute of Physics Publishing)
- [4] Wang M (ed) 2015 *Industrial Tomography* (Cambridge: Woodhead Publishing)
- [5] Brandstätter B, Holler G and Watzenig D 2003 Reconstruction of inhomogeneities in fluids by means of capacitance tomography *COMPEL* **22** 508–19
- [6] Li Y, Yang W, Xie C, Huang S, Wu Z, Tsamakis D and Lenn C 2013 Gas/oil/water flow measurement by electrical capacitance tomography *Meas. Sci. Technol.* **24** 074001
- [7] Isaksen O, Dico A S and Hammer E A 1994 A capacitance-based tomography system for interface measurement in separation vessels *Meas. Sci. Technol.* **5** 1262–71
- [8] Jaworski A J and Dyakowski T 2001 Application of electrical capacitance tomography for measurement of gas–solids flow characteristics in a pneumatic conveying system *Meas. Sci. Technol.* **12** 1109–19
- [9] Jama G A, Klinzing G E and Rizk F 2000 An investigation of the prevailing flow patterns and pressure fluctuation near the pressure minimum and unstable conveying zone of pneumatic transport systems *Powder Technol.* **112** 87–93
- [10] Yang W 2010 Design of electrical capacitance tomography sensors *Meas. Sci. Technol.* **21** 04200
- [11] Hansen P C 1998 *Rank-Deficient and Discrete Ill-Posed Problems: Numerical Aspects of Linear Inversion* (Philadelphia, PA: SIAM)
- [12] Cui Z, Wang Q, Xue Q, Fan Q, Zhang L, Cao L, Sun B, Wang H and Yang W 2016 A review on image reconstruction algorithms for electrical capacitance/resistance tomography *Sensor Rev.* **36** 429–45
- [13] Neumayer M, Zangl H, Watzenig D and Fuchs A 2011 Current reconstruction algorithms in electrical capacitance tomography *New Developments and Applications in Sensing Technology* (Berlin: Springer) pp 65–106
- [14] Watzenig D and Fox C 2009 A review of statistical modelling and inference for electrical capacitance tomography *Meas. Sci. Technol.* **20** 052002

- [15] Kaipio J P and Somersalo E 2004 *Statistical and Computational Inverse Problems (Applied Mathematical Sciences)* 1st edn (New York: Springer)
- [16] Smolik W T et al 2017 Single-shot high-voltage circuit for electrical capacitance tomography *Meas. Sci. Technol.* **28** 025902
- [17] Wang B, Ji H, Huang Z and Li H 2005 A high-speed data acquisition system for ECT based on the differential sampling method *IEEE Sens. J.* **5** 308–12
- [18] Wegleiter H, Fuchs A, Holler G and Kortschak B 2008 Development of a displacement current-based sensor for electrical capacitance tomography applications *J. Flow Meas. Instrum.* **19** 241–50
- [19] Huang A, Cao Z, Sun S, Lu F and Xu L 2019 An agile electrical capacitance tomography system with improved frame rates *IEEE Sens. J.* **19** 1416–25
- [20] Chen D, Yang W and Pan M 2010 The dynamic response of a Butterworth low-pass filter in an ac-based electrical capacitance tomography system *Meas. Sci. Technol.* **21** 105505
- [21] Cui Z, Wang H, Chen Z, Xu Y and Yang W 2011 A high-performance digital system for electrical capacitance tomography *Meas. Sci. Technol.* **22** 055503
- [22] Fan Z and Gao R X 2012 A frequency selection scheme for increased imaging speed in ECT *Proc. IEEE Int. Conf. on Imaging Systems and Techniques* (Manchester: Manchester University Press) pp 616–21
- [23] Yang W Q and York T A 1999 New AC-based capacitance tomography system *IEE Proc.: Sci. Meas. Technol.* **146** 47–53
- [24] Yang W Q 1996 Hardware design of electrical capacitance tomography systems *Meas. Sci. Technol.* **7** 225–323
- [25] Da M J Silva and Hampel U 2009 A field-focusing imaging sensor for fast visualization of multiphase flows *Meas. Sci. Technol.* **20** 104009
- [26] Yang W Q, Stott A L and Beck M S 1994 High frequency and high resolution capacitance measuring circuit for process tomography *IEE Proc., Circuits Devices Syst.* **141** 215–19
- [27] Yang W Q 1996 Calibration of capacitance tomography systems: a new method for setting system measurement range *Meas. Sci. Technol.* **7** L863–7
- [28] Bolton G T, Korchinsky W J and Waterfall R C 1998 Calibration of capacitance tomography systems for liquid–liquid dispersions *Meas. Sci. Technol.* **9** 1797
- [29] Yang W Q, Chondronasios A, Nattrass S, Nguyen V T, Betting M, Ismail I and McCann H 2004 Adaptive calibration of a capacitance tomography system for imaging water droplet distribution *Flow Meas. Instrum.* **15** 249–58
- [30] Mohamad E J, Rahim R A, Ling L P, Rahiman M H F, Bin Marwah O M F and Ayob N M N 2012 Segmented capacitance tomography electrodes: a design and experimental verifications *IEEE Sens. J.* **12** 1589–98
- [31] Pozar D M 2011 *Microwave Engineering* 3rd edn (New York: Wiley)
- [32] Flatscher M, Neumayer M, Bretterkieber T and Wegleiter H 2016 Front-end circuit modeling for low-Z capacitance measurement applications *Proc. IEEE Int. Instrumentation and Measurement Technology Conf. (Taipei, Taiwan)* pp 1400–5
- [33] Flatscher M, Neumayer M and Bretterkieber T 2018 Impedance matched front-end circuitry for electrical capacitance tomography systems *Proc. 9th World Confess on Industrial Process Tomography (Bath, UK)* pp 537–45
- [34] Niknejad A 2007 Terminated transmission line *Electromagnetics for high-Speed Analog and Digital Communication Circuits* (Cambridge: Cambridge University Press) ch 12, pp 348–57 (section 12.4)
- [35] Neumayer M, Flatscher M and Bretterkieber T 2018 Front end instrumentation modeling of electrical tomography systems *Proc. 9th World Confess on Industrial Process Tomography (Bath, UK)* pp 423–32
- [36] Neumayer M and Steiner G 2009 Impact of wave propagation effects in electrical tomography *Proc. 17th Conf. on the Computation of Electromagnetic (Florianopolis, Brazil)* pp 414–5
- [37] Kryszyn J, Wróblewski P, Stosio M, Wanta D, Olszewski T and Smolik W T 2017 Architecture of EVT4 data acquisition system for electrical capacitance tomography *Measurement* **101** 28–39
- [38] Lu D C, Wu J X and Shao F Q 2013 The research of high voltage electrical capacitance tomography system *Appl. Mech. Mater.* **303** 896–9
- [39] Dorf R C 1997 Resistors *The Electrical Engineering Handbook* 2nd edn (Boca Raton, FL: CRC Press) ch 1, pp 5–15 (section 1.1)
- [40] Razavi B 2017 MOS device capacitances *Design of Analog CMOS Integrated Circuits* 2nd edn (New York: McGraw-Hill) ch 2, pp 27–31 (section 2.4.2)
- [41] Brocco L M, McCormick S P and Allen J 1988 Macromodeling CMOS circuits for timing simulation *IEEE Trans. Comput.-Aided Des. Integr. Circuits Syst.* **7** 1237–49
- [42] Horowitz P and Hill W 2015 Inverting amplifier *The Art of Electronics* 3rd edn (Cambridge: Cambridge University Press) ch 4, pp 225–6 (section 4.2.1)
- [43] Flatscher M, Neumayer M and Bretterkieber T 2018 Holistic analysis for electrical capacitance tomography front-end electronics *J. Phys.: Conf. Ser.* **1065** 092008
- [44] Tietze U, Schenk C and Gamm E 2008 High-frequency equivalent circuits *Electronic Circuits* 2nd edn (Berlin: Springer) ch 26, pp 1283–9 (section 26.1)
- [45] Grubmüller M, Schweighofer B and Wegleiter H 2014 Characterization of a resistive voltage divider design for wideband power measurements *Proc. IEEE Sensors (Valencia, Spain)* pp 1332–5
- [46] Rosa E B and Grover F W 1912 Formulas and tables for the calculation of mutual and self-inductance *Bull. Bur. Stand.* **8** 1–237
- [47] Wegleiter H, Fuchs A, Holler G and Kortschak B 2005 Analysis of hardware concepts for electrical capacitance tomography applications *Proc. IEEE Sensors (Irvine, CA)* pp 688–91
- [48] Rohde A and Schwarz 2019 ZVL3 vector network analyzer (Accessed on: 11 April 2019) ([www.rohde-schwarz.com/product/zvl3-productstartpage\\_63493-9015.html](http://www.rohde-schwarz.com/product/zvl3-productstartpage_63493-9015.html))
- [49] Cheng D 2006 Wave characteristics on finite transmission lines *Field and Wave Electromagnetics* 2nd edn (Reading, MA: Addison-Wesley) ch 9 (section 9.4)
- [50] Ballou G M (ed) 2008 Transmission techniques: wire and cable *Handbook for Sound Engineers* 4th edn (Burlington, MA: Focal Press) ch 14, pp 432–3 (section 14.24)